Supporting information

Unity of opposites: stabilisation of cationic M_6 metal cluster and anionic Lindqvist-type polyoxotungstate in hybrid salts and synergism in photodegradation of organic pollutants

Anton A. Petunin, Arina V. Tomilenko, Darya V. Evtushok, Anton A. Ivanov, Alexey A. Ryadun, Taisiya S. Sukhikh, Igor P. Asanov, Michael A. Shestopalov, Yuri A. Vorotnikov*

Nikolaev Institute of Inorganic Chemistry SB RAS, 3 Acad. Lavrentiev Ave., 630090 Novosibirsk, Russia, E-mail: vorotnikov@niic.nsc.ru

Instrumentation

Centrifugation was achieved by a Changsha Xiangzhi, model CLN-16 centrifuge equipped with rotor 6×50 mL, operating at 6000 rpm. SEM (scanning electron microscopy) images were obtained using Hitachi TM3000 TableTop SEM. Energy-dispersive X-ray spectroscopy (EDS) was performed on a Hitachi TM3000 TableTop SEM with a Bruker QUANTAX 70 EDS equipment with results reported as the ratio of the heavy elements. Elemental analyses (CHN/S) were obtained using a EuroVector EA3000 Elemental Analyser. FTIR spectra were recorded on a Bruker Vertex 80 as KBr disks. X-ray powder diffraction (XRPD) patterns were recorded on a Tongda TD-3700 diffractometer (CuKα radiation λ = 1.54178 Å, Ni filter, linear detector Dectris Mythen2 1D). The thermal properties were studied on a Thermo Microbalance TG 209 F1 Iris from 25 to 950°C at the heating rate of 10°C min^{-1} in He flow (30 mL min^{-1}). XPS analysis was executed employing an X-ray photoelectron spectrometer FLEXPS equipped with an electron energy analyzer Phoibos 150 and delay line electron detector. All measurements were conducted using monochromatic Al Kα irradiation. The electron pass energy utilized was 20 eV, and to counteract the charging effect, low-energy electron beam irradiation was applied to the samples. The calibration of binding energies was referenced to an internal standard with the C1s peak set at 285.0 eV. Distinguishing the contributions from different atoms was achieved through spectral fitting utilizing mixed Lorentzian-Gaussian symmetrical components in CasaXPS.

Optical diffuse reflectance spectra (DRS) were recorded on a Shimadzu UV-vis-NIR 3101 PC spectrophotometer equipped with an integrating sphere and interpreted based on the Kubelka-Munk theory. Corrected luminescence spectra were recorded on a Fluorolog 3 Horiba Jobin Yvon spectrometer with a cooled PC177CE-010 photon detection module (R2658 photomultiplier) and two Czerny-Turner double monochromators. The measurements were conducted using both continuous (450 W) and pulsed (FWHM pulse time 3 μs, 50 W) Xe-lamps. Absolute value of luminescence quantum yield (λ_{ex} = 400 nm) was obtained using Quanta-φ device of Fluorolog 3.

Ultrasonic treatment was conducted utilizing a "Sapphire" ultrasonic bath with an ultrasound power of 150 W and a frequency of 35 kHz. The particle size and morphology were characterized by TEM (transmission electron microscopy) with a Libra 120 microscope (Zeiss) at an acceleration voltage of 60 kV. Free image software "ImageJ" was used for particle size measuring. Visible-light irradiation in photodegradation experiments was performed using a spot light source L8253 (Hamamatsu) with a range of 400-800 nm and intensity of approximately ~40 mW cm^{-2}. UV-light irradiation was performed with a Hamamatsu Photonics light-emitting-diode (LED) head unit L11921-400 (λ = 365±5 nm, ~13 mW cm^{-2}) used with a LED controller C11924-211. Absorption spectra were recorded on an Agilent Cary 60 spectrophotometer.

Crystal structure determination

Single-crystal X-ray diffraction data were collected at 150 K with a Bruker D8 Venture diffractometer with a CMOS PHOTON III detector and IμS 3.0 microfocus source (MoK$_\alpha$ radiation, λ = 0.71073 Å, collimating Montel mirrors). Data reduction was performed routinely via APEX 3 suite.[1] The structures were solved using the ShelXT[2] and were refined using ShelXL[3] programs assisted by Olex2 GUI.[4] All hydrogen atoms for the organic part were located in the geometrical positions and refined in the riding model. Structures of **1b** and **2** reveal disorder of one of the [W$_6$O$_{19}$]$^{2-}$ anions over six equivalent positions, which were refined in rigid body approximation. Single-crystal XRD patterns of compounds **1b** and **2** showed rod-like diffuse scattering along *c** direction (Fig. S4 and S5), indicates the anions are not statistically disordered, but feature some long-range order. Due to this feature, the structures reveal high residual electron density and high R$_1$ factor. However, the quality of the structures is enough for discussing their main parameters. Table S1 summarizes crystallographic data, while CCDC 2402991-2402993 contains the supplementary crystallographic data for this paper. The data can be obtained free of charge from the Cambridge Crystallographic Data Centre via www.ccdc.cam.ac.uk/data_request/cif.

Emission quenching experiments

Prior to measurements DMSO solutions of $[\{M_6I_8\}(DMSO)_6](NO_3)_4$ and $(Bu_4N)_2[W_6O_{19}]$ were mixed giving a specific cluster/POM molar ratios – 1/2, 1/4, and 1/8 for M = Mo and 1/0.5, 1/1, 1/1.5, and 1/2 for M = W. The absorption of the resulting solutions at 355 nm was <0.1. Emission spectra of the solutions were recorded using an Agilent Cary Eclipse Fluorescence Spectrophotometer. Using the data obtained, Stern-Volmer (SV) plots were plotted in the form of I_0/I *vs* C_{POM}, and Stern-Volmer constants (K_{SV}) were determined from linear approximation of the plots in accordance with well-known equation $I_0/I = 1 + K_{SV}[Q]$. I_0 is emission intensity in the absence of quencher and $[Q]$ is quencher concentration.

DFT calculations

Density functional theory (DFT) calculations were carried out for $[\{M_6I_8\}(DMSO)_6]^{4+}$ (M = Mo, W) cluster cations and $[W_6O_{19}]^{2-}$ anion in theADF2023 software package.[5-6] Optimization of geometric parameters of the ionic compounds was performed with the B3LYP hybrid density functional,[7] Grimme D4 (EEQ) dispersion correction,[8] and all-electron TZP basis set.[9] Calculated IR-spectra of the compounds do not contain imaginary frequencies. Single-point calculations were performed with the B3LYP hybrid density functional, GrimmeD4 (EEQ) dispersion correction, and all-electron TZ2P basis set. Zero-order regular approximation (ZORA)[10] for scalar relativistic effects and the conductor-like screening model (COSMO)[11] for the DMSO environment were used in all calculations.

Stability study

To study the stability of **1b** and **2** under harsh conditions in aqueous media, the samples (100 mg) were placed in 10 mL of water. One group was ultrasonicated for 2 h (T = 60°C), while another group was irradiated with white light for 2 h. Third group was kept in 1 M H_2SO_4 for 24 h. After the experiments, the powders were centrifuged, washed with water, and dried in ambient conditions. XRPD patterns were recorded to evaluate the preservation of the samples.

Photocatalytic experiments

The photocatalytic activity of **1b** and **2** in photodegradation process was evaluated under white light irradiation using rhodamine B (RhB) as model dye. 6, 12, or 24 mg of the catalysts were dispersed in 6 mL of H_2O under ultrasonic treatment (15 min). After that, 6 mL of RhB solution (20 mg L^{-1}, 4.17×10^{-5} M) was added to the dispersion (V_{total} = 12 mL, C_{RhB} = 2.1×10^{-5} M) and stirred in dark for 1 h to reach adsorption-desorption equilibrium. The resulting mixture was irradiated with white light (400-800 nm, ~40 mW cm^{-2}) or UV light (for C_{cat} = 1 mg mL, λ = 365±5 nm, ~13 mW cm^{-2}) under constant stirring. An aliquot (1 mL) was collected every 2.5 min, centrifuged twice to remove catalyst, and then a UV-vis spectrum of the isolated solution was recorded. The decrease in dye concentration was monitored by its characteristic optical absorbance at 553 nm. The rate constants (k_{eff}) of the reactions were determined as zero-order kinetics by linear approximation of the C *vs* t plot, where C is the concentration of RhB at specific t, t is the time at which aliquots of solutions were taken.

Photocatalytic experiments with scavengers

To assess the activity of reactive species, standard photocatalytic experiments were carried out in the presence of scavengers (C = 10 mM): $Na_2C_2O_4$ (h^+), $K_2Cr_2O_7$ (e^-), and ethylene glycol (EG, $OH^\bullet$). To evaluate the contribution of $O_2^{\bullet-}$, the reaction mixture was deaerated by bubbling argon gas for 10 minutes. The relative activity (RA) was calculated using Equation (1).

$$RA = \frac{k_{eff}(scav)}{k_{eff}(NS)} \times 100\%$$

where $k_{eff}(scav)$ is the effective rate constant in the presence of a specific scavenger and $k_{eff}(NS)$ is the effective rate constant in the absence of a scavenger. The rate constants were calculated using the same method as described earlier.

Cyclic experiments

The water solution (12 mL) containing RhB (2.1×10^{-5} M) and the catalyst (1 g L^{-1}) was irradiated under constant stirring with white light for 40 min per run. After each run, whole dispersion was centrifuged, and UV-vis spectrum of the solution was recorded. Then centrifuged powders were washed with water and redispersed in 6 mL of water. 6 mL of RhB was added to the dispersion to adjust initial concentration of dye and catalyst. In total, 5 cycles of photodegradation were conducted. After the cycling experiments, the materials were characterized by XRPD to assess the preservation of the sample composition.
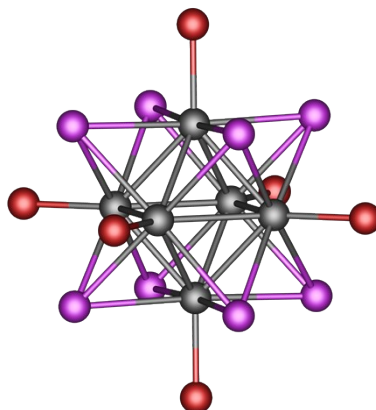
Fig. S1. General structure of octahedral M_6 iodide cluster. Color code: gray – metal (Mo or W), pink – iodine, red – apical ligands
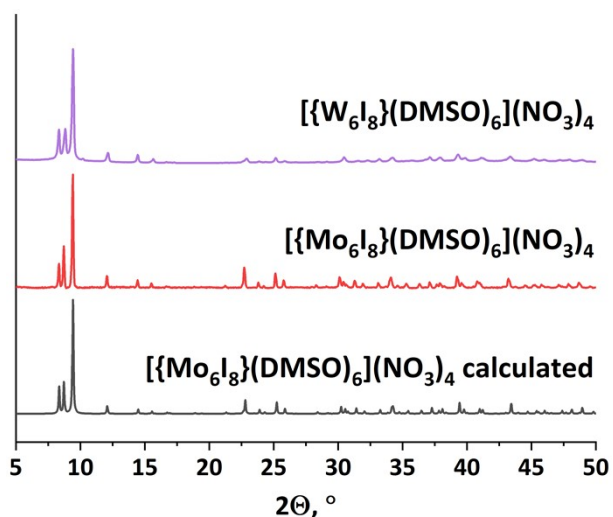

**Fig. S2.** XRPD patterns of [{M_6I_8}(DMSO)$_6$](NO$_3$)$_6$.
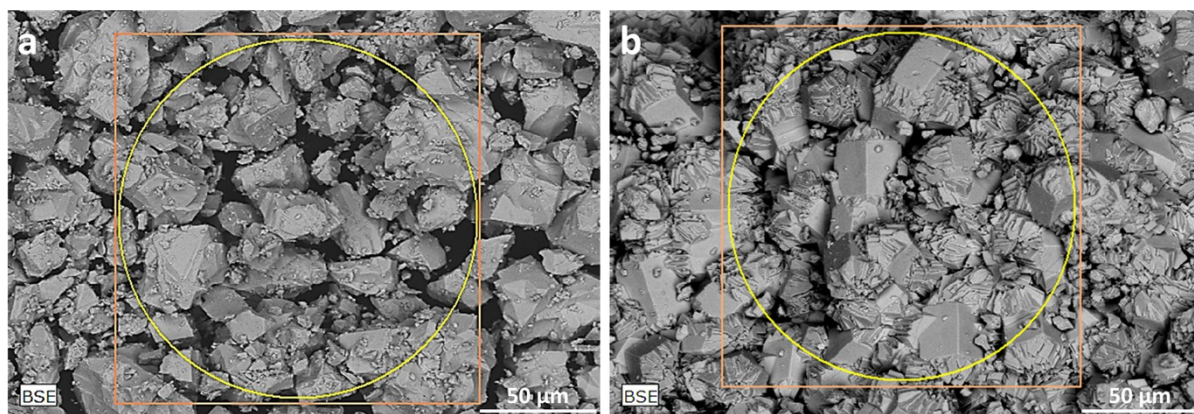
Fig. S3. SEM images of **1b** (a) and **2** (b).

**Table S1.** Crystallographic data, data collection and refinement parameters for **1a**, **1b**, and **2**.

	1a	1b	2
Empirical formula	$C_{12}H_{36}I_8Mo_6O_{44}S_6W_{12}$	$C_{12}H_{36}I_8Mo_6O_{44}S_6W_{12}$	$C_{12}H_{36}I_8O_{44}S_6W_{18}$
Formula weight	4873.81	4873.81	5401.27
Temperature (K)	150(2)	150(2)	150(2)
Crystal size (mm³)	0.17 × 0.04 × 0.04	0.08 × 0.06 × 0.04	0.07 × 0.03 × 0.03
Crystal system	Triclinic	Trigonal	Trigonal
Space group	$P\,\overline{1}$	$P\,\overline{3}1c$	$P\,\overline{3}1c$
Z	2	2	2
Unit cell dimensions			
a (Å)	12.2540(3)	15.2662(7)	15.2684(8)
b (Å)	12.4723(3)	15.2662(7)	15.2684(8)
c (Å)	24.5269(6)	17.4257(12)	17.4210(13)
α (°)	75.5510(10)	90	90
β (°)	78.8620(10)	90	90
γ (°)	75.8240(10)	120	120
Volume (Å³)	3484.48(15)	3517.1(4)	3517.1(5)
$D_{calcd.}$ (g·cm⁻³)	4.645	4.602	5.100
μ. mm⁻¹	24.556	24.328	33.062
θ range (°)	3.464 – 59.15	3.08 – 55.854	3.08 – 54.964
Indices ranges	−17 ≤ h ≤ 17 −17 ≤ k ≤ 17 −34 ≤ l ≤ 34	−20 ≤ h ≤ 20 −20 ≤ k ≤ 20 −22 ≤ l ≤ 22	−19 ≤ h ≤ 19 −19 ≤ k ≤ 19 −22 ≤ l ≤ 22
Reflections collected	61607	71158	39783
Independent reflections	19519	2813	2709
Data / restraints / parameters	19519/12/844	2813/577/277	2709/463/277
$R[F^2 > 2\sigma(F^2)]$	$R_1 = 0.0363$ $wR_2 = 0.0773$	$R_1 = 0.1158$ $wR_2 = 0.2625$	$R_1 = 0.1113$ $wR_2 = 0.2674$
$R(F^2)$ (all data)	$R_1 = 0.0497$ $wR_2 = 0.0842$	$R_1 = 0.1204$ $wR_2 = 0.2651$	$R_1 = 0.1264$ $wR_2 = 0.2772$
Goodness-of-fit on F^2	1.031	1.205	1.203
$\Delta\rho_{max}$. $\Delta\rho_{min}$ (e·Å⁻³)	1.99 / -2.50	9.05/-5.01	11.58/-4.33
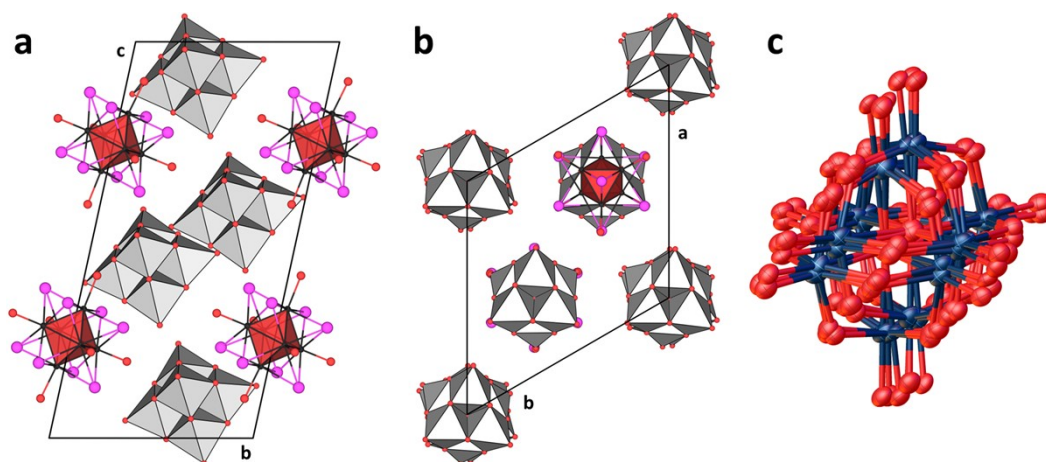
Fig. S4. Unit cells of **1a** (a) and **1b** (b). Apical DMSO ligands and the disorder of POM are omitted for clarity. Disorder of one of the POM anions in **1b** over six proximate equivalent positions (c).

0kl	*h0l*	*hk0*
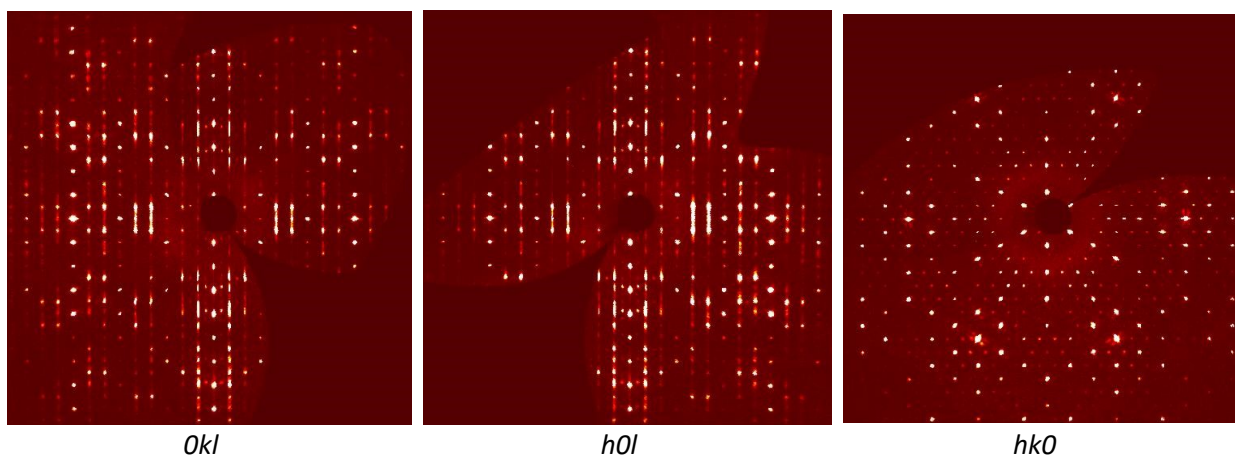
Fig. S5. Reciprocal space reconstructions for compound **1b**, showing *0kl, h0l,* and *hk0* layers (the thickness of the layers of 0.10 Å). Along *c** direction, diffuse rod-like scattering is observed, which implies some long-range order of the anions in one dimension along *c**.

0kl	*h0l*	*hk0*
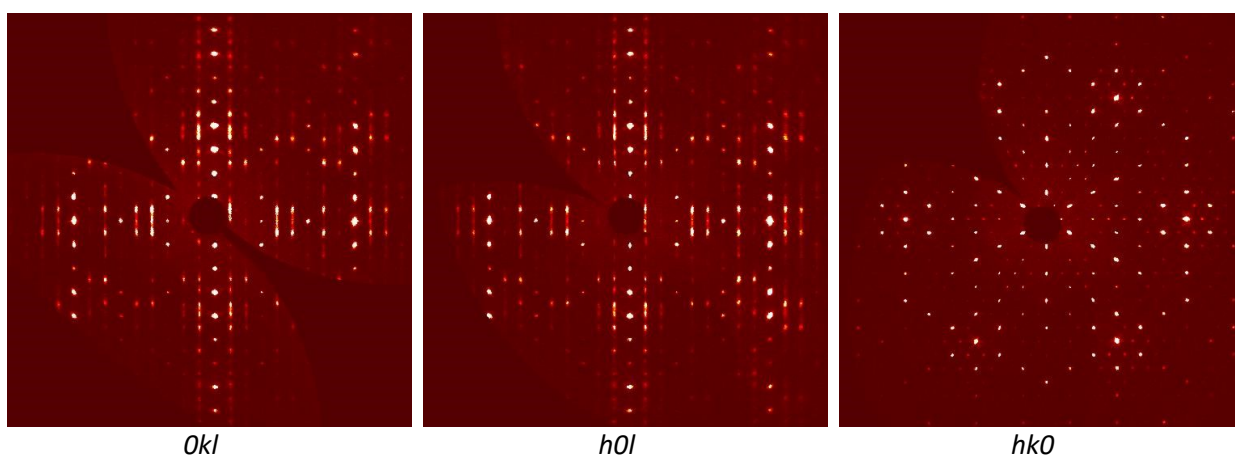
Fig. S6. Reciprocal space reconstructions for compound **2**, showing *0kl, h0l,* and *hk0* layers (the thickness of the layers of 0.10 Å). Along *c** direction, diffuse rod-like scattering is observed, which implies some long-range order of the anions in one dimension along *c**.
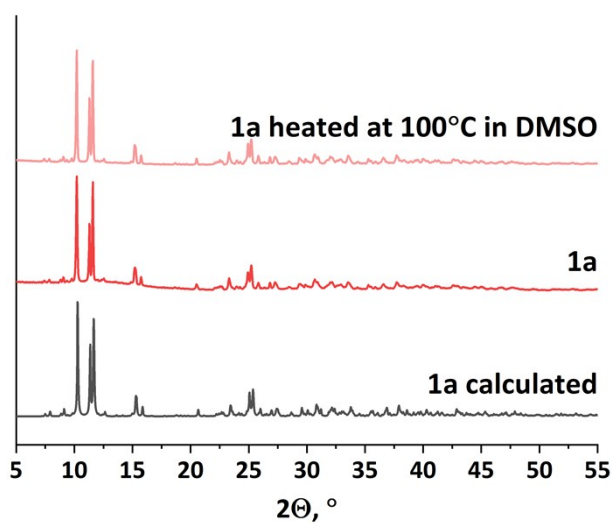
Fig. S7. XRPD patterns of initial **1a** and **1a** heated in DMSO at 100°C compared to calculated diffractograms.
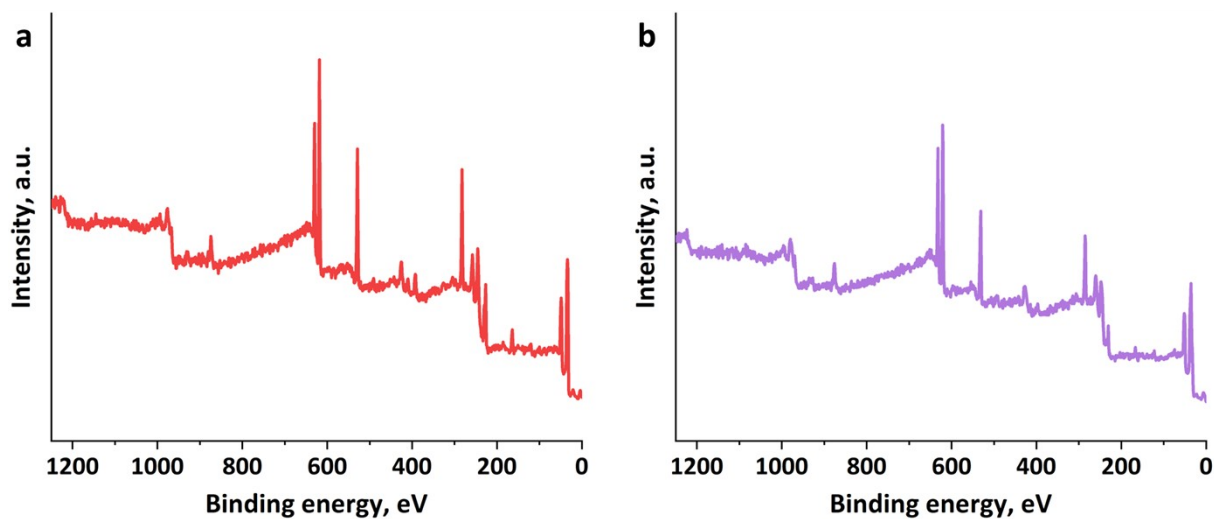
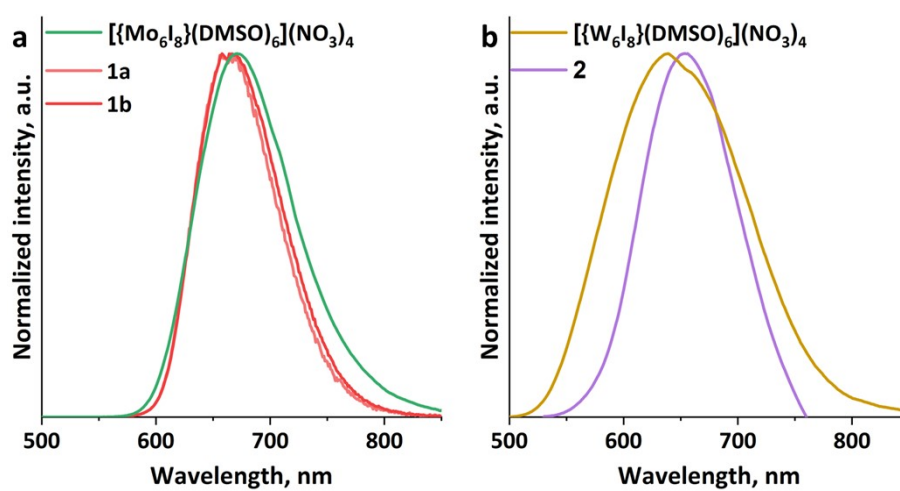**Fig. S8.** XPS survey spectra of **1b** (a) and **2** (b).

Fig. S9. Comparison of emission spectra of **1a/1b** vs $[\{Mo_6I_8\}(DMSO)_6](NO_3)_4$ (a) and **2** vs $[\{W_6I_8\}(DMSO)_6](NO_3)_4$ (b).
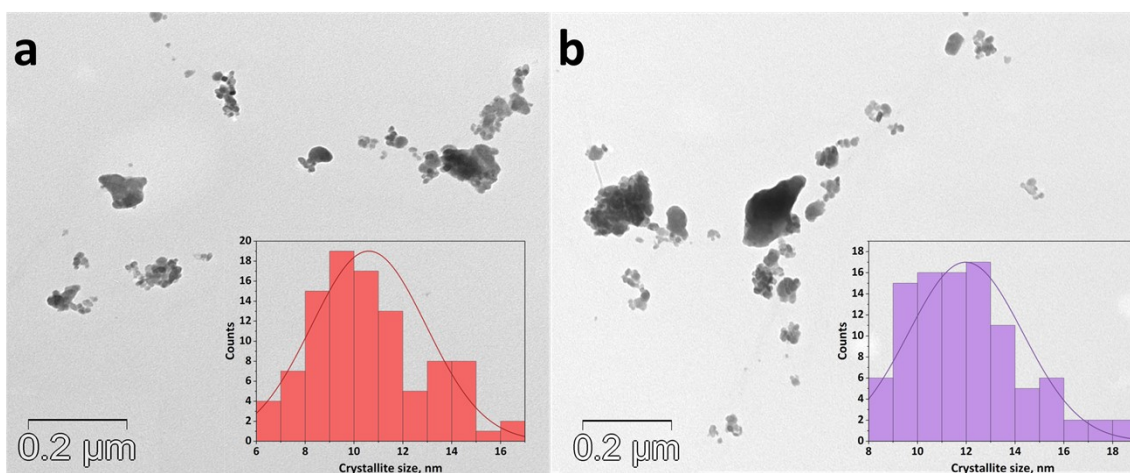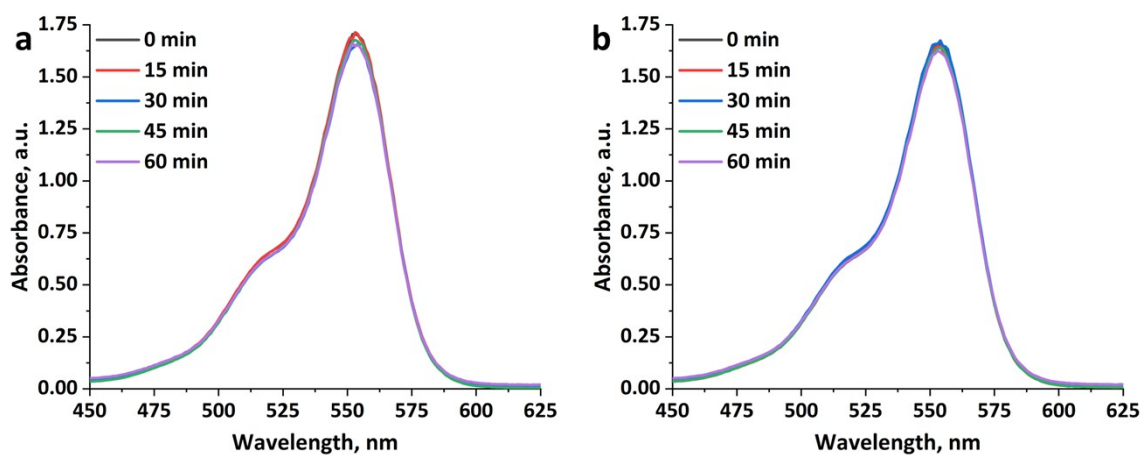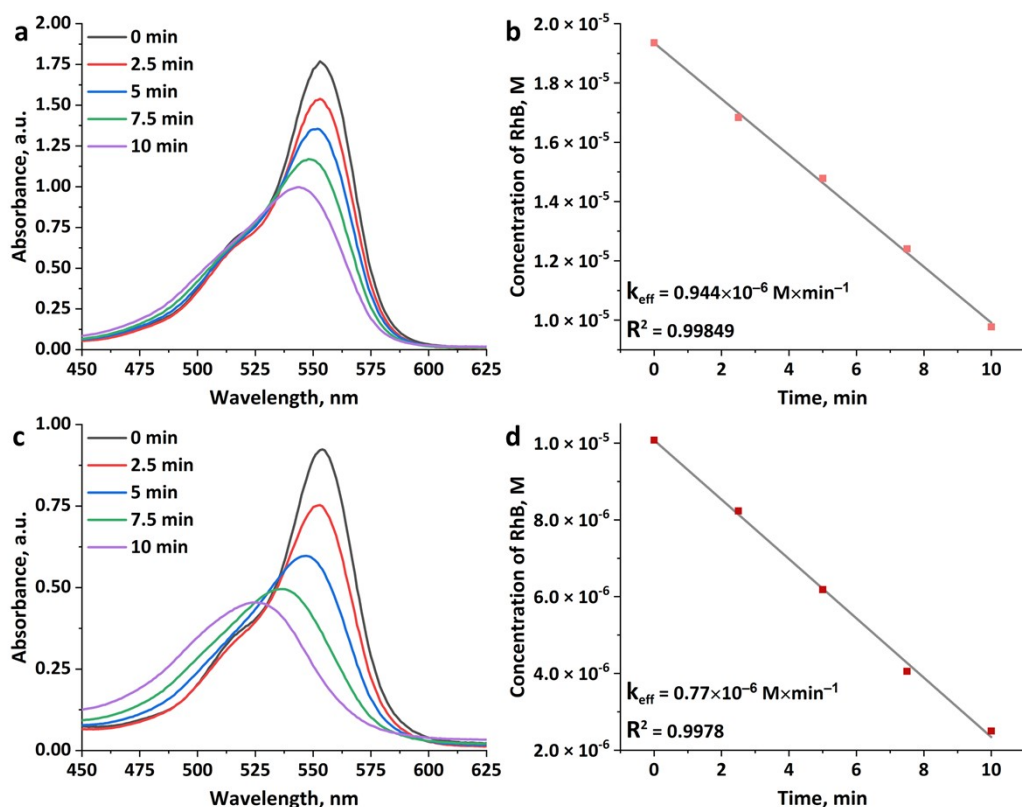

Fig. S10. TEM images of **1b** (a) and **2** (b). Inserts are particle size analysis.
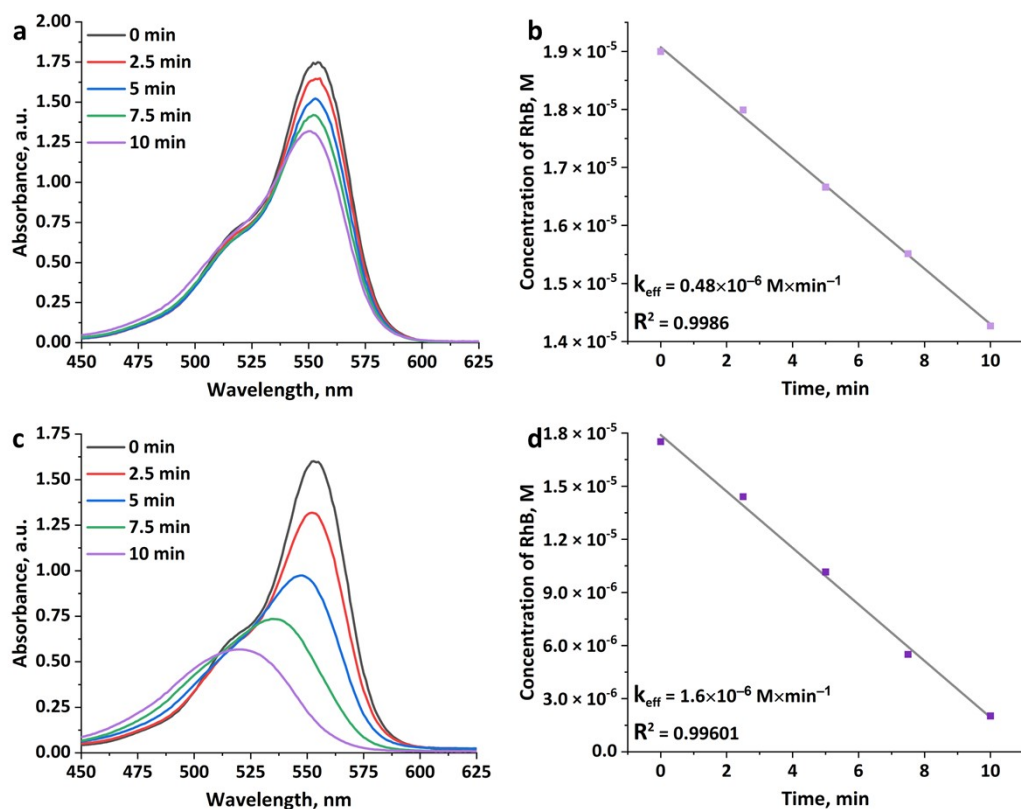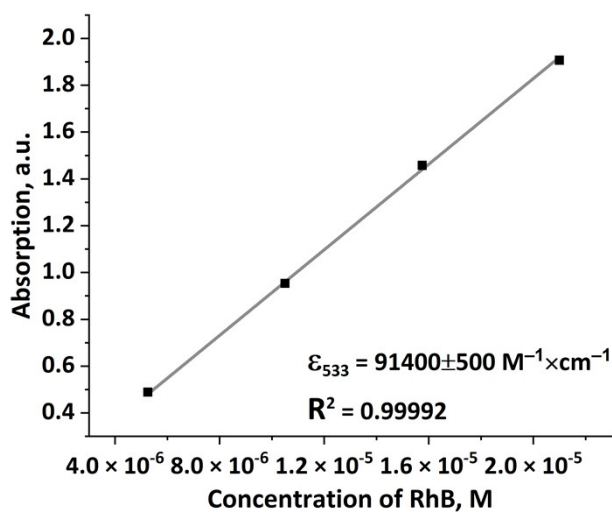
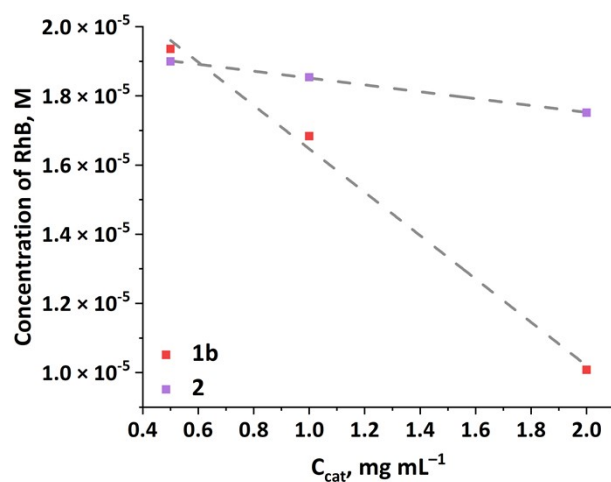**Fig. S11.** RhB sorption by **1b** (a) and **2** (b) in the dark.

Fig. S12. Absorption spectra of RhB solution before and after irradiation with white light (λ = 400-800 nm) in the presence of **1b** at different concentrations – 0.5 (a) and 2 (c) g L^{-1}. Linear approximation of C *vs* t plots used for determination of k_{eff} for **1b** (b, d).

Fig. S13. Absorption spectra of RhB solution before and after irradiation with white light (λ = 400-800 nm) in the presence of **2** at different concentrations – 0.5 (a) and 2 (c) g L^{-1}. Linear approximation of C *vs* t plots used for determination of k_{eff} for **2** (b, d).
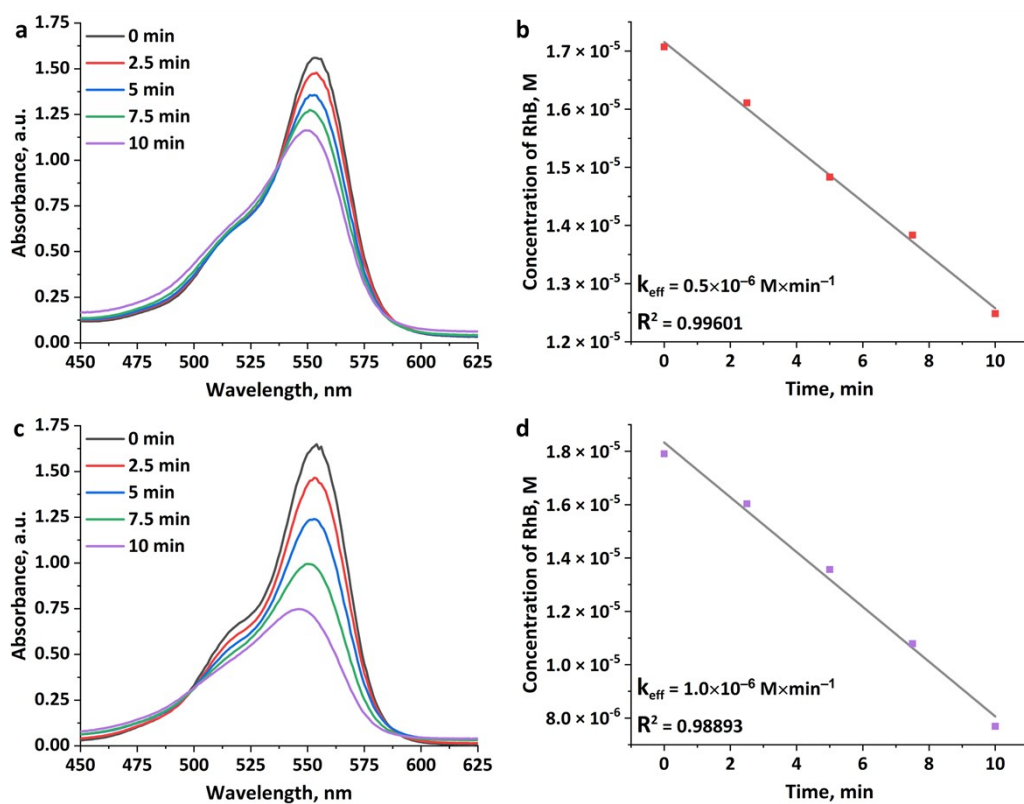

Fig. S14. Determination of RhB absorption coefficient at 533 nm.

Fig. S15. The dependence of concentration of catalyst on the concentration of RhB after 1 h of sorption.

Fig. S16. Absorption spectra of RhB solution before and after irradiation with UV light (λ = 365±5 nm) in the presence of **1b** (a) and **2** (c) during different time intervals. Linear approximation of C vs t plots used for determination of k_{eff} for **1b** (b) and **2** (d).
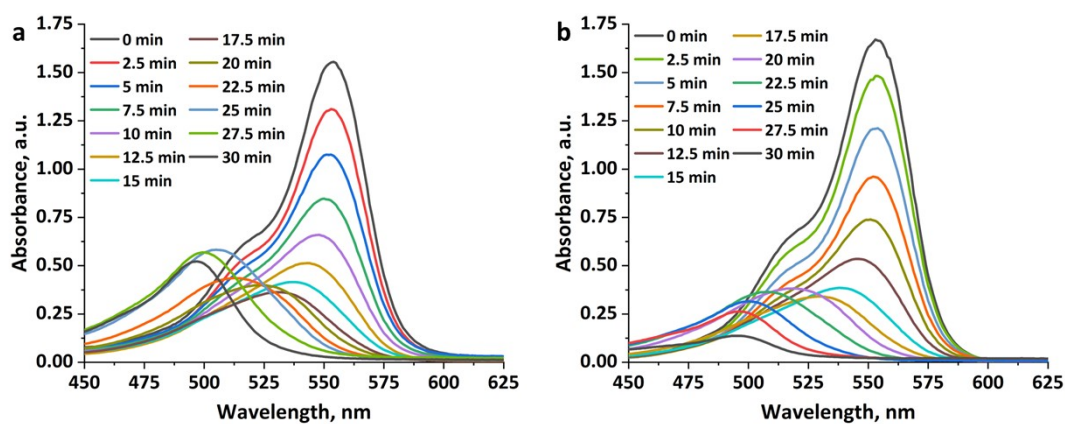
Fig. S17. Decomposition of RhB in the presence of **1b** (a) and **2** (b) during 30 min.

Table S2. Effective rate constants (k_{eff}) of RhB photodegradation under white light (λ = 400-800 nm).

| C_{cat}, g L^{-1}	$k_{eff} \times 10^6$, M×min^{-1}	
	1b	**2**
0.5	0.94	0.48
1	1.0 (0.5*)	1.1 (1.0*)
2	0.77	1.6

*activity under UV irradiation (λ = 365±5 nm, ~13 mW cm^{-2})

Table S3. Comparison of the efficiency of various heterogenous photocatalysts in photodegradation of RhB under visible light.

Catalyst	Wavelength, nm (power)	C_{RhB}, M×10^{-5}	Catalyst dose, g L^{-1}	Volume, mL	Irradiation time, min	Degradation rate, %	Ref
[{Mo$_6$I$_8$}(DMSO)$_6$][W$_6$O$_{19}$]$_2$ (**1b**)	400-800 nm (~40 mW cm^{-2})	2.1	1	12	30	~100	This work
[{W$_6$I$_8$}(DMSO)$_6$][W$_6$O$_{19}$]$_2$ (**2**)					25	~100	
{Mo$_6$I$_8$}$^{0.1}$@TiO$_2$	Natural sunlight (~30–35 mW cm^{-2})	0.5	0.25	80	45	~100	12
{W$_6$I$_8$}$^{0.1}$@TiO$_2$						~100	
{Mo$_6$Br$_8$}^{10}@N-TiO$_2$	400-800 nm (~40 mW cm^{-2})	0.5	0.8	50	2	44	13
{Mo$_6$I$_8$}^{10}@N-TiO$_2$						58	
NaBiO$_3$	Xenon lamp (750 W)	4.2	1	100	30	~97	14
Bi$_{24}$O$_{31}$Cl$_{10}$	Xenon lamp (250 W)	1	1	100	180	98.44	15
N-TiO$_2$/rGO	Xenon lamp	2.1	20 mg*	-	90	78.29	16
Bi$_2$WO$_6$	Xenon lamp (30 mW cm^{-2})	1	0.5	100	60	>95	17
Zn$_{1-x}$Ni$_x$O	Xenon lamp (500 W)	2.1	0.25	100	150	~100	18
(C$_{10}$N$_2$H$_9$)$_2$[H$_2$P$_2$Mo$_5$O$_{23}$] [Cu(C$_{10}$N$_2$H$_8$)$_2$]·18H$_2$O	Xenon lamp (1000 W)	6.3	0.3	50	300	89.6	19
PW$_{11}$Mn/D301R	Metal halide lamp (200 W)	2.1	0.4	250	40	100	20
Ag$_4$V$_2$O$_7$	Xenon lamp (350 W)	2	2	50	180	97.56	21
Nd-POMCene	Xenon lamp (300 W)	6.3	0.15	100	60	100	22
H$_3$PW$_{12}$O$_{40}$/TiO$_2$	Xenon lamp (400 W)	10	1.25	200	60	98	23
Ag$_3$PO$_4$/POM/GO$^{\#}$	Xenon lamp (500 W)	1	0.5	100	15	100	24
Pb$_3$Nb$_4$O$_{13}$/Fumed SiO$_2$	Xenon lamp (300 W)	2.5	3	100	60	~100	25

*Total volume is not specified
#POM is molybdophosphoric silver
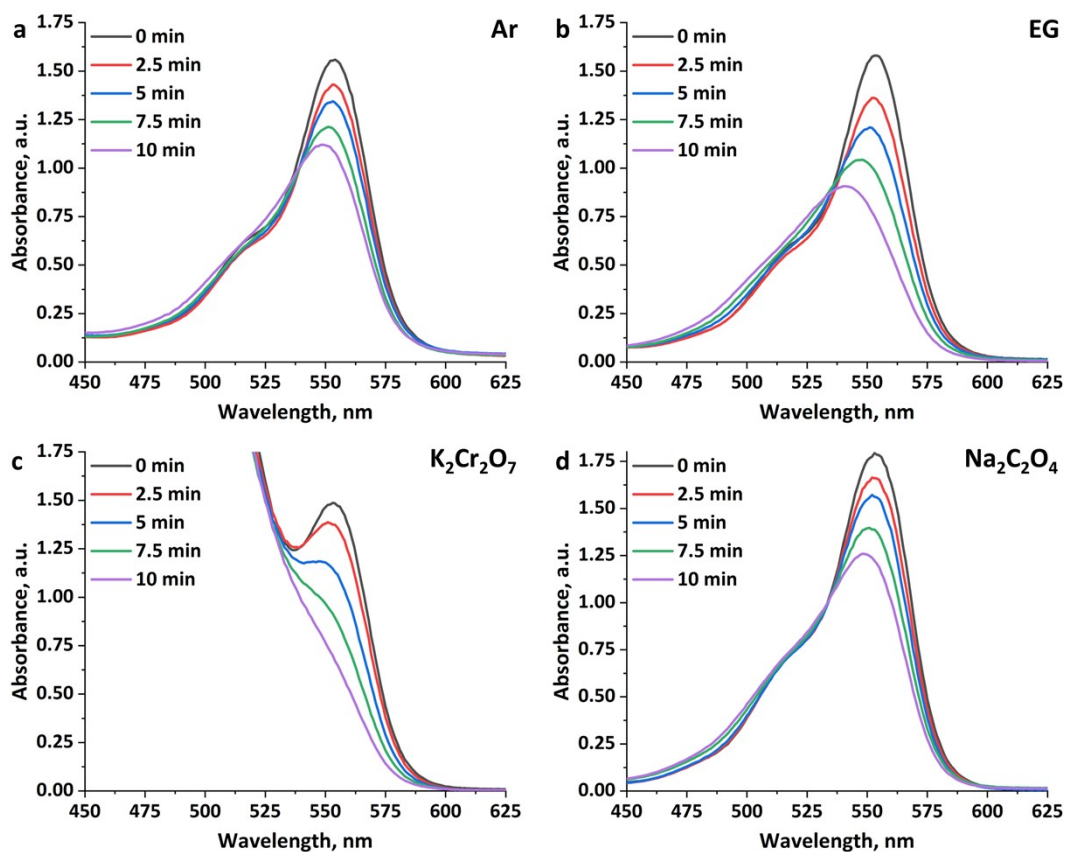
Fig. S18. Absorption spectra of RhB solution before and after irradiation with white light (λ = 400-800 nm) in the presence of **1b** and various scavengers – Ar (a), ethylene glycol (b), $K_2Cr_2O_7$ (c), $Na_2C_2O_4$ (d).
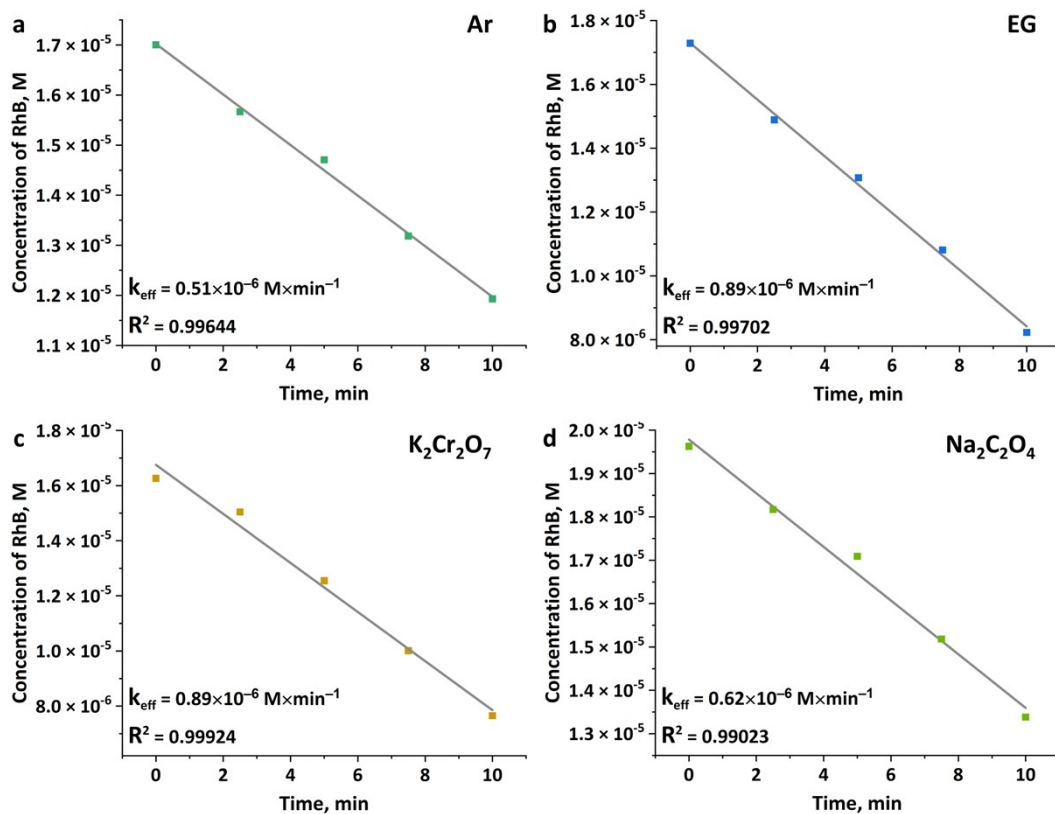
Fig. S19. C vs. time plots for photocatalytic degradation of RhB by **1b** in the presence of different scavengers – Ar (a), ethylene glycol (b), $K_2Cr_2O_7$ (c), $Na_2C_2O_4$ (d).
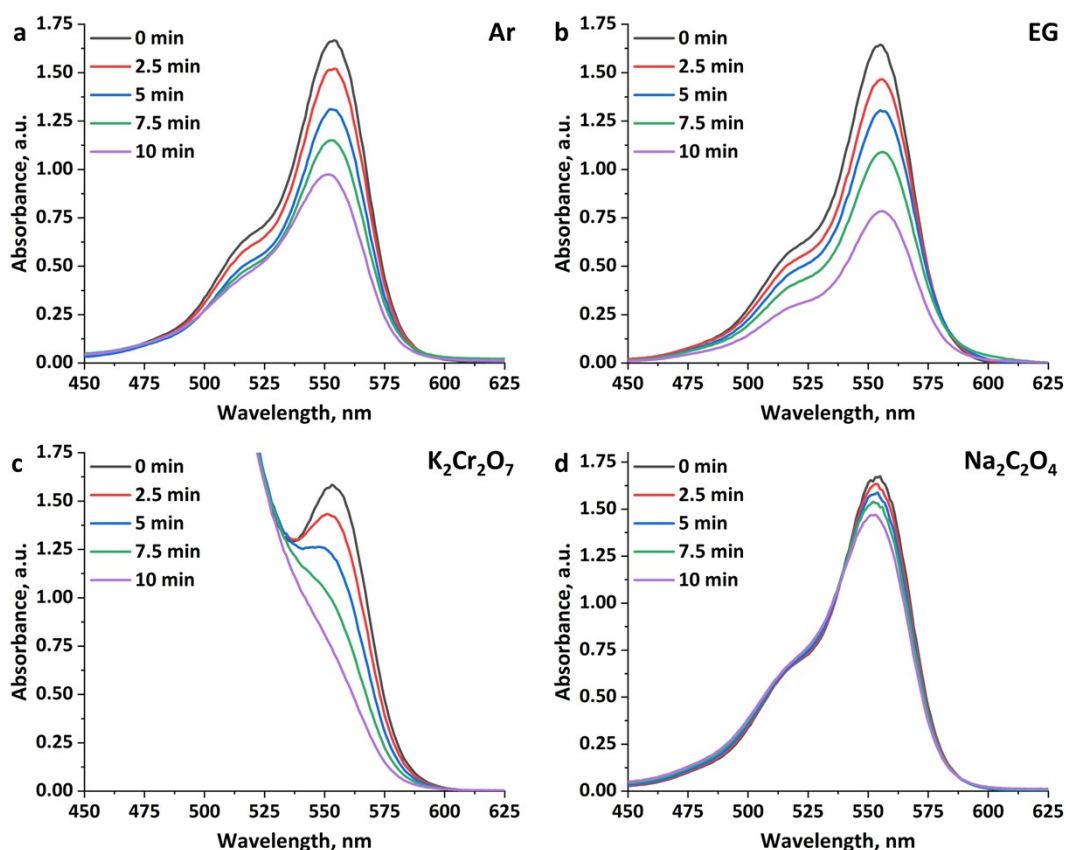
Fig. S20. Absorption spectra of RhB solution before and after irradiation with white light (λ = 400-800 nm) in the presence of **2** and various scavengers – Ar (a), ethylene glycol (b), $K_2Cr_2O_7$ (c), $Na_2C_2O_4$ (d).
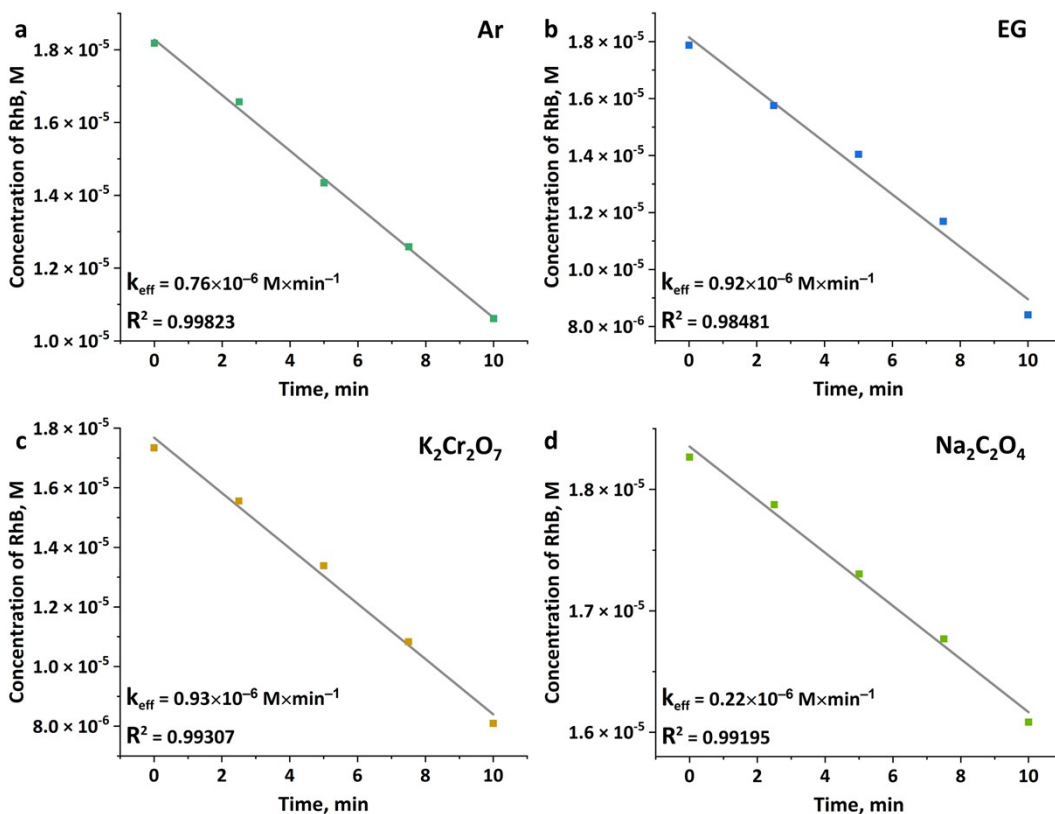

Fig. S21. C vs. time plots for photocatalytic degradation of RhB by **2** in the presence of different scavengers – Ar (a), ethylene glycol (b), $K_2Cr_2O_7$ (c), $Na_2C_2O_4$ (d).
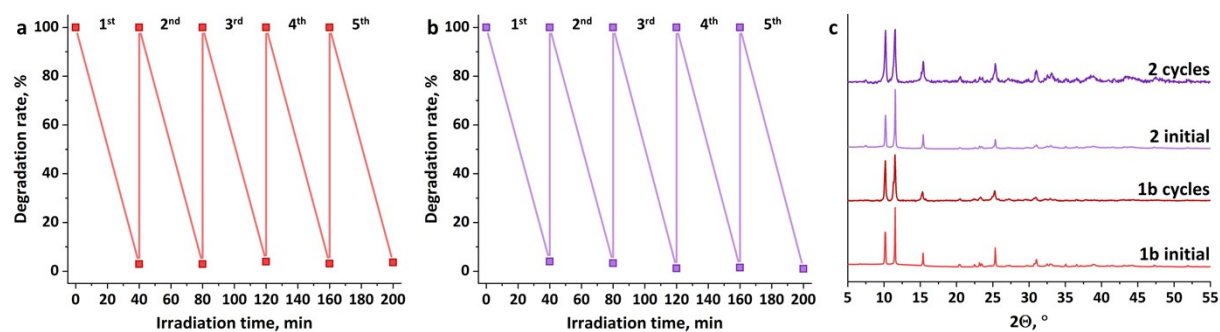
Fig. S22. Cycling of **1b** (a) and **2** (b) in RhB photocatalytic degradation. XRPD diffractograms of materials after 5 cycles of RhB degradation (c).
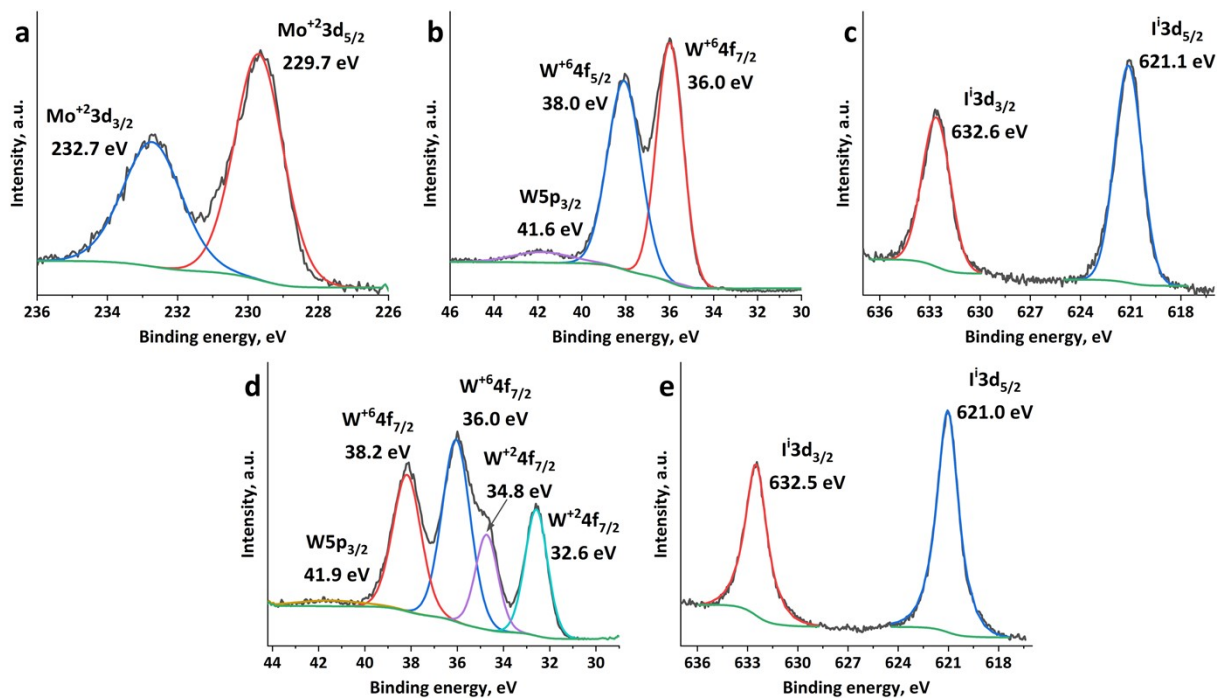
Fig. S23. High-resolution XPS spectra of Mo3d (a), W4f (b), I3d (c) core levels in **1b** and W4f (d), I3d (e) core levels in **2** for materials after 5 cycles of RhB degradation.

References

1.   *Bruker Apex3 software suite: Apex3, SADABS-2016/2 and SAINT 8.40a; Publisher: Bruker AXS Inc., Madison, WI, USA, 2017.*

2.   Sheldrick, G., SHELXT - Integrated Space-Group and Crystal-Structure Determination. *Acta Crystallogr. Sect. A* **2015,** *71*, 3-8. https://doi.org/10.1107/S2053273314026370

3.   Sheldrick, G., Crystal Structure Refinement with SHELXL. *Acta Crystallogr. Sect. C* **2015,** *71*, 3-8. https://doi.org/10.1107/S2053229614024218

4.   Dolomanov, O. V.; Bourhis, L. J.; Gildea, R. J.; Howard, J. A. K.; Puschmann, H., OLEX2: A Complete Structure Solution, Refinement and Analysis Program. *J. Appl. Crystallogr.* **2009,** *42*, 339-341. https://doi.org/10.1107/S0021889808042726

5.   te Velde, G.; Bickelhaupt, F. M.; Baerends, E. J.; Fonseca Guerra, C.; van Gisbergen, S. J. A.; Snijders, J. G.; Ziegler, T., Chemistry with ADF. *J. Comput. Chem.* **2001,** *22* (9), 931-967. https://doi.org/10.1002/jcc.1056

6.   *ADF 2023.1, SCM, Theoretical Chemistry, Vrije Universiteit, Amsterdam, The Netherlands.* http://www.scm.com *(accessed 2024-06-13).*

7.   Stephens, P. J.; Devlin, F. J.; Chabalowski, C. F.; Frisch, M. J., Ab Initio Calculation of Vibrational Absorption and Circular Dichroism Spectra Using Density Functional Force Fields. *J. Phys. Chem.* **1994,** *98* (45), 11623-11627. https://doi.org/10.1021/j100096a001

8.   Caldeweyher, E.; Ehlert, S.; Hansen, A.; Neugebauer, H.; Spicher, S.; Bannwarth, C.; Grimme, S., A Generally Applicable Atomic-Charge Dependent London Dispersion Correction. *J. Chem. Phys.* **2019,** *150* (15), ARTN 154122. https://doi.org/10.1063/1.5090222

9.   Van Lenthe, E.; Baerends, E. J., Optimized Slater-Type Basis Sets for the Elements 1–118. *J. Comput. Chem.* **2003,** *24* (9), 1142-1156. https://doi.org/10.1002/jcc.10255

10.   van Lenthe, E.; Ehlers, A.; Baerends, E.-J., Geometry Optimizations in the Zero Order Regular Approximation for Relativistic Effects. *J. Chem. Phys.* **1999,** *110* (18), 8943-8953. https://doi.org/10.1063/1.478813

11.   Pye, C. C.; Ziegler, T., An Implementation of the Conductor-Like Screening Model of Solvation Within the Amsterdam Density Functional Package. *Theor. Chem. Acc.* **1999,** *101* (6), 396-408. https://doi.org/10.1007/s002140050457

12.   Marchuk, M. V.; Asanov, I. P.; Panafidin, M. A.; Vorotnikov, Y. A.; Shestopalov, M. A., Nano TiO_2 and Molybdenum/Tungsten Iodide Octahedral Clusters: Synergism in UV/Visible-Light Driven Degradation of Organic Pollutants. *Nanomaterials* **2022,** *12* (23), ARTN 4282. https://doi.org/10.3390/nano12234282

13.   Olawoyin, C. O.; Vorotnikov, Y. A.; Asanov, I. P.; Shestopalov, M. A.; Vorotnikova, N. A., N-Doped Titania Nanoparticles Containing Mo_6 Bromide and Iodide Clusters: Activity in Photodegradation of Rhodamine B and Tetracycline. *Chemosphere* **2024,** *366*, ARTN 143531. https://doi.org/10.1016/j.chemosphere.2024.143531

14. Yu, K.; Yang, S.; He, H.; Sun, C.; Gu, C.; Ju, Y., Visible Light-Driven Photocatalytic Degradation of Rhodamine B over $NaBiO_3$: Pathways and Mechanism. *J. Phys. Chem. A* **2009,** *113* (37), 10024-10032. https://doi.org/10.1021/jp905173e

15. Bikerchalen, S.; Akhsassi, B.; Bakiz, B.; Villain, S.; Taoufyq, A.; Guinneton, F.; Gavarri, J. R.; Benlhachemi, A., Photocatalytic Degradation of Rhodamine B Dye over Oxygen-Rich Bismuth Oxychloride $Bi_{24}O_{31}Cl_{10}$ Photocatalyst under UV and Visible Light Irradiation: Pathways and Mechanism. *J. Phys. Chem. Sol.* **2025,** *196*, ARTN 112342. https://doi.org/10.1016/j.jpcs.2024.112342

16. Utami, M.; Wang, S.; Fajarwati, F. I.; Salsabilla, S. N.; Dewi, T. A.; Fitri, M., Enhanced Photodegradation of Rhodamine B Using Visible-Light Sensitive $N-TiO_2$/rGO Composite. *Crystals* **2023,** *13* (4), ARTN 588. https://doi.org/10.3390/cryst13040588

17. Fu, H.; Pan, C.; Yao, W.; Zhu, Y., Visible-Light-Induced Degradation of Rhodamine B by Nanosized Bi_2WO_6. *J. Phys. Chem. B* **2005,** *109* (47), 22432-22439. https://doi.org/10.1021/jp052995j

18. Yin, Q.; Qiao, R.; Li, Z.; Zhang, X. L.; Zhu, L., Hierarchical Nanostructures of Nickel-Doped Zinc Oxide: Morphology Controlled Synthesis and Enhanced Visible-Light Photocatalytic Activity. *J. Alloys Compd.* **2015,** *618*, 318-325. https://doi.org/10.1016/j.jallcom.2014.08.087

19. Liang, Z.; Cheng, H.; Zhang, X.; Mao, Q., Two Polyoxometalates Based on {P_2Mo_5} Catalysts: Synthesis, Characterization, and Photocatalytic Degradation of RhB. *J. Mol. Liq.* **2023,** *377*, ARTN 121483. https://doi.org/10.1016/j.molliq.2023.121483

20. Hua, Y.; Chen, G.; Xu, X.; Zou, X.; Liu, J.; Wang, B.; Zhao, Z.; Chen, Y.; Wang, C.; Liu, X., Comparative Study of Homogeneous and Heterogeneous Photocatalytic Degradation of RhB under Visible Light Irradiation with Keggin-Type Manganese-Substituted Catalysts. *J. Phys. Chem. C* **2014,** *118* (17), 8877-8884. https://doi.org/10.1021/jp409082q

21. Zhou, D.; Chen, Y.-X.; Yuan, X.-Y.; Lu, Y.; Zhang, M.; Liu, J.-K., Self-Induced Synthesis Under Neutral Conditions and Novel Visible Light Photocatalytic Activity of $Ag_4V_2O_7$ Polyoxometalate. *New J. Chem.* **2021,** *45* (21), 9569-9581. https://doi.org/10.1039/D1NJ01390D

22. Zhang, X.; Xu, Y.; Guo, R.; Chen, Y.; Zhang, Y., Highly Ordered 2D Honeycomb Polyoxometalate Clusterphene for Efficient Photocatalytic Degradation of Organic Pollutants: Mechanism, Pathways, and Toxicity Evaluation. *Appl. Surf. Sci.* **2024,** *656*, ARTN 159675. https://doi.org/10.1016/j.apsusc.2024.159675

23. Yang, Y.; Wu, Q.; Guo, Y.; Hu, C.; Wang, E., Efficient Degradation of Dye Pollutants on Nanoporous Polyoxotungstate–Anatase Composite Under Visible-Light Irradiation. *J. Mol. Catal. A: Chem.* **2005,** *225* (2), 203-212. https://doi.org/10.1016/j.molcata.2004.08.031

24. Liu, G.; Zhao, X.; Zhang, J.; Liu, S.; Sha, J., Z-Scheme Ag_3PO_4/POM/GO Heterojunction with Enhanced Photocatalytic Performance for Degradation and Water Splitting. *Dalton Trans.* **2018,** *47* (17), 6225-6232. https://doi.org/10.1039/C8DT00431E

25.   Li, X.; Ye, J., Photocatalytic Degradation of Rhodamine B over $Pb_3Nb_4O_{13}$/Fumed SiO_2 Composite under Visible Light Irradiation. *J. Phys. Chem. C* **2007,** *111* (35), 13109-13116. https://doi.org/10.1021/jp072752m